






Control and tunability of magnetic bubble states in multilayers with strong perpendicular magnetic anisotropy at ambient conditions

Ruslan Salikhov ^{1,*} Fabian Samad ^{1,2} Sri Sai Phani Kanth Arekapudi ² Rico Ehrler,² Jürgen Lindner,¹ Nikolai S. Kiselev ^{3,†} and Olav Hellwig ^{1,2,‡}

¹*Institute of Ion Beam Physics and Materials Research, Helmholtz-Zentrum Dresden-Rossendorf, Bautzner Landstrasse 400, 01328 Dresden, Germany*

²*Institute of Physics, Chemnitz University of Technology, Reichenhainer Strasse 70, 09107 Chemnitz, Germany*

³*Peter Grünberg Institute and Institute for Advanced Simulation, Forschungszentrum Jülich and JARA, 52425 Jülich, Germany*



(Received 28 February 2022; revised 7 July 2022; accepted 18 July 2022; published 1 August 2022)

The reversal of magnetic bubble helicity through topologically trivial transient states provides an additional degree of freedom that promises the development of multidimensional magnetic memories. A key requirement for this concept is the stabilization of bubble states at ambient conditions on application-compatible substrates. In the present work, we demonstrate a stabilization routine for remanent bubble states in high perpendicular magnetic anisotropy [Co(0.44 nm)/Pt(0.7 nm)]_X, $X = 48, 100$, and 150 multilayers on Si/SiO₂ substrates by exploring the effect of external magnetic fields (H_m) of different strength and angles (θ) with respect to the film surface normal. By systematic variation of these two parameters, we demonstrate that remanent bubble density and mean bubble diameter can be carefully tuned and optimized for each sample. Our protocol based on magnetometry only reveals the densest remanent bubble states at $H_m = 0.87H_s$ (H_s is the magnetic saturation field) and $\theta = 60^\circ\text{--}75^\circ$ for all X with a maximum of 3700 domains/100 μm^2 for the $X = 48$ sample. The experimental observations are supported by micromagnetic simulations, taking into account the nanoscale lateral grain structure of multilayers synthesized by magnetron sputter deposition, and thus helping to understand the different densities of the bubble states found in these systems.

DOI: [10.1103/PhysRevB.106.054404](https://doi.org/10.1103/PhysRevB.106.054404)

I. INTRODUCTION

Noncollinear magnetic textures, such as magnetic domain walls, vortices, bubbles, and skyrmions, are currently the subject of intense research. New concepts, which allow efficient manipulation of these objects at the nanoscale, fuel unrelenting interest in this topic. Due to the relatively weak coupling of magnetic spins to the lattice of a host material (thus avoiding large heat losses), these magnetic textures have the potential for applications in nonvolatile and energy-efficient memory and logic devices, e.g., architectures based on artificial neural networks for multidimensional computation [1–3]. In particular, magnetic skyrmions [4] have been suggested for spintronic applications, utilizing the controlled motion of these particlelike magnetic nanotextures [5–11].

From the viewpoint of topology, magnetic skyrmions, stabilized by Dzyaloshinskii-Moriya interaction (DMI), are identical to type I magnetic bubbles [4,12–14]. The main difference is that skyrmions may have only one energetically favorable chirality, while magnetic bubbles have identical energies for both chiralities [15–21]. In this respect, magnetic bubbles have an additional degree of freedom to switch between two energetically equivalent states. The transition

between bubbles of opposite chirality typically occurs via a topologically trivial transient state, known as type II bubbles, characterized by an “onionlike” magnetic texture and a nonzero net magnetization in the plane of the film hosting the bubble [12,22,23].

The presence of two topological states with opposite chirality and an additional topologically trivial state leads to different dynamical responses of the magnetic bubbles to external driving forces [4,12,15–19,21,24]. Thereby, the magnetic bubbles may provide extra functionality compared to skyrmions stabilized by bulk or interfacial DMI. As has been shown earlier, the type I bubbles can be switched to type II bubbles back and forth on a timescale of 100 ps [4,15,16]. Moreover, recent studies suggest a new strategy for magnetic memories, employing current-driven bubble helicity reversal [25,26].

This strategy requires steps towards stabilization of dipolar bubbles in metallic multilayers (MLs) at zero field, where the control of a well-defined and strong DMI interaction is not required anymore. Such bubble states have been reported in Co/Pt and Fe/Gd MLs with symmetric interfaces [27–30]. The approach suggested in Refs. [20,27,28], however, requires a particular design of the ML to balance the contribution of the perpendicular magnetic anisotropy (PMA), K_u , and the demagnetizing field energy density, $K_d = \frac{1}{2}\mu_0 M_s^2$ (μ_0 is the vacuum magnetic permeability and M_s is the saturation magnetization), which in the case of multidomain states additionally scales with the ML thickness. Noticeably, stable

* r.salikhov@hzdr.de

† n.kiselev@fz-juelich.de

‡ o.hellwig@hzdr.de

bubble states in all these studies have been obtained in MLs with a low quality factor, $Q < 1$, which represents the ratio $Q = K_u/K_d$. Furthermore, the magnetic field protocol used for stabilizing bubble states is specific to each material, depending on its magnetic energy characteristics [27–30]. This brings significant complexity for the stabilization of zero-field magnetic bubbles in metallic MLs.

In earlier studies, it has been demonstrated that by applying out-of-plane fields to [Co/Pt]₅₀ MLs with different Co thickness, a remanent dense bubble domain state can only be formed at Co thicknesses above 2.5 nm [27]. This implies that at smaller Co thicknesses, where the material is characterized by $Q > 1$, it is more difficult to obtain dense bubble states, and an interconnected labyrinth stripe state is more common. In this work, we report a reliable approach for the stabilization of dense magnetic bubble states at zero magnetic field and room temperature in PMA MLs with symmetric interfaces and $Q > 1$. Thus, we extend the material class, which can possess metastable bubbles at ambient conditions. Our approach is based on the search for an optimal magnetic field at different tilt angles (θ) with respect to the ML normal, where the nucleation of the bubble state occurs, and it can be identified after returning to remanence. Varying the tilt angle and applied magnetic field in the same ML, we observe a wide diversity of states with remanent bubbles of different diameters, densities, and arrangements. In three samples of significantly different thickness, we find that the optimal range of maximal fields and tilt angles providing the densest bubble states is nearly identical. Thereby, the presented approach appears suitable for a large family of MLs synthesized by magnetron sputter deposition.

The paper is organized as follows. We first outline the experimental techniques, the sample preparation details, and its magnetic and structural properties. Then we demonstrate our concept of remanent bubble state stabilization, and we discuss the density and size distribution characteristics of the bubbles. Finally, we show the results of micromagnetic simulations, providing insight into the sample morphology and the resulting micromagnetic parameters that impact the observed bubble domain formation and its characteristic bubble size distribution at remanence.

II. MATERIALS AND METHODS

To demonstrate that a dense bubble state can be stabilized in MLs with a high quality factor, $Q > 1$, we select [(Co(0.44 nm)/Pt(0.7 nm))_X], $X = 48, 100, \text{ and } 150$ MLs, with strong PMA ($Q \approx 1.6$). The MLs films were fabricated at room temperature by dc magnetron sputter deposition at 0.4 Pa Ar atmosphere in an ultrahigh vacuum system ATC 2200 from AJA International Inc. Si wafers with a 100-nm-thick thermally oxidized (SiO₂) layer were used as substrates. Prior to the multilayer deposition, a 1.5 nm Ta layer was deposited for adhesion purposes. A subsequent 20 nm Pt layer serves as a seed in order to obtain a preferred Co/Pt (0001)/(111) texture, which supports better growth and larger PMA [28]. The sample was finally capped by a 2 nm Pt layer to avoid surface oxidation. Magnetic measurements were performed using a commercial Microsense EZ7 vibrating sample magnetometer (VSM), equipped with an electromag-

net, which delivers up to 1.8 T magnetic field, and with a $\theta = 360^\circ$ rotational stage. In the following, $\theta = 0^\circ$ corresponds to the out-of-plane (OOP) and $\theta = 90^\circ$ to the in-plane (IP) geometry. Magnetic domain imaging was performed using a Bruker Dimension Icon magnetic force microscope (MFM). Magnetic images were analyzed using Gwyddion software, which employs a magnetic contrast marking (watershed) algorithm and thus allows an accurate calculation of the domain density and area of a particular magnetization direction. All MFM images were recorded at room temperature and zero magnetic field. The saturation magnetization of all samples was measured using the VSM and calculated to be $M_s = 0.77 \pm 0.07$ MA/m. The PMA constant was determined from the area between IP and OOP hysteresis loops (see Fig. S1 in the Supplemental Material [31]) to $K_u \approx 0.6$ MJ/m³, yielding $Q \approx 1.6$.

The ML nature of the samples was structurally characterized by x-ray reflectivity (XRR) using a Cu K_α radiation-source diffractometer (Rigaku SmartLab XG). The specular reflectivity curve for all samples reveals an intense ML Bragg peak (see Fig. S2 in the Supplemental Material [31]) indicating a good quality of the Co/Pt superlattice. The $X = 100$ and 150 samples display a larger surface roughness as compared to the thinner $X = 48$ sample. This is due to the columnar grain growth of the MLs, which causes the development of a correlated ML roughness, thus increasing the overall surface roughness with increasing film thickness [32–37]. However, the off-specular reflectivity peak intensity increases with X , thus confirming a sustained good ML periodicity even in thicker samples with increased surface roughness. Furthermore, the peak width decreases with the thickness, reflecting a good vertical coherence of the multilayering through the entire system.

III. EXPERIMENT AND DISCUSSION

Figure 1(a) shows representative magnetic hysteresis loops measured in the IP and OOP geometries for the sample with $X = 150$. The OOP magnetization requires a smaller field for magnetic saturation as compared to the IP loop, which is due to the large PMA. Both loops exhibit small remanent magnetization at zero magnetic field, $M_r = M(0)$. The nonzero M_r in the OOP geometry results from the imbalance of the volumes of “up” and “down” domains forming a mazelike pattern shown in the top-left inset in Fig. 1(a) [23]. With increasing the OOP field towards saturation, mazelike domains decay into isolated stripes, which decay further into isolated bubble domains [38]. At a critical field, H_{bc} , slightly below the saturation field, bubble domains collapse. When one reduces the field back to zero, the isolated bubble domains experience strip-out instability and expand back into labyrinth domains [23,38]. The imbalance between “up” and “down” domains originates from the so-called configuration hysteresis effect [23] and depends on the magnetic history, namely the direction and strength of the previously applied fields [27,30]. On the other hand, the nonzero M_r in the IP geometry is mainly attributed to the polarization of the Bloch-type domain walls (DWs) in the direction of the external magnetic field [39]. In the case of a tilted magnetic field, $0^\circ < \theta < 90^\circ$, both effects—the ratio of “up” and “down” domains

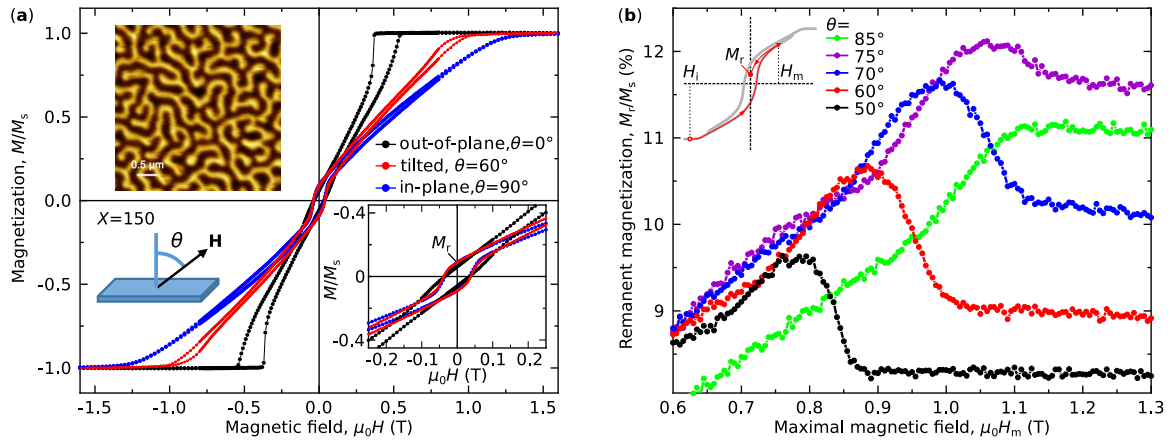


FIG. 1. (a) The magnetic hysteresis loops measured with magnetic field applied parallel (black circles), perpendicular (blue circles), and at a tilted angle $\theta = 60^\circ$ (red circles) with respect to the [Co (0.44 nm)/Pt (0.7 nm)]₁₅₀ multilayer surface normal. The bottom-right inset is an enlarged view of the corresponding hysteresis loops at small magnetic fields. The top-left inset displays a magnetic force microscope (MFM) image of the sample recorded at zero field after OOP saturation. The maze-like stripe domain state is evident in the MFM image. (b) Normalized remanent magnetization (M_r/M_s) as a function of previously applied magnetic field (H_m) in the DCR protocol for different field angles ($\theta = 50^\circ, 60^\circ, 70^\circ, 75^\circ, 85^\circ$) with respect to the film normal. In the DCR protocol, the sample was magnetically saturated at negative fields, and then a positive field H_m was applied at an angle θ . In the next step, the field was set back to zero, and magnetization was measured at remanence. A characteristic peak of the remanent magnetization at each presented field angle is clearly evident for angles up to 75° , but it vanishes when approaching 90° , i.e., an in-plane field orientation.

and the domain-wall polarization—contribute to the remanent magnetization. It is reasonable to expect that the in-field behavior of the system in the presence of both OOP and IP components of the external field will also differ from the limiting cases of $\theta = 0^\circ$ and 90° .

As has been shown earlier [20,40,41], the IP component of the field supports the formation of parallel stripe domains, whereas the OOP component contracts the stripe domains until they pinch off into topologically trivial type II bubbles. Such bubbles form a dense irregular lattice shortly before the field reaches the critical value H_{bc} . When the bubble domains form a dense enough structure, then, as the external field is decreased back to remanence, labyrinth or stripe domain formation is suppressed due to the high magneto-static repulsion between the tightly packed bubble domains and the missing space for expansion into stripes [42,43]. Hence, the dense bubble state remains stable even at zero field. To realize this scenario, one must know (i) the optimal tilt angle of the external magnetic field, and (ii) the optimal magnetic field strength at which stripe domains pinch off into bubble domains. For this, we employ an approach based on measurements of the remanent magnetization (M_r) as a function of the maximal external field H_m applied at different tilt angles θ . We use a similar magnetic field protocol as commonly applied in first-order reversal curve (FORC) acquisition, which has been proven to be a valuable technique for the identification of skyrmionic states in DMI MLs [44–46].

Figure 1(b) shows the behavior of the normalized remanent magnetization (M_r/M_s) as a function of H_m for some selected field angles. The measurement protocol [which we refer to as the DC-remnance (DCR) protocol] is explained by the scheme depicted in the top-left inset in Fig. 1(b) and is composed of the following steps. First, the tilt angle θ is adjusted and the sample is initially saturated at strong negative field

$\mu_0 H_i = -1.8$ T. Then, a positive field H_m is applied, and after that the field is gradually (within a few seconds) reduced to zero. Then M_r is measured at $H = 0$ and plotted as a function of H_m . We varied H_m between $0 < \mu_0 H_m < 1.6$ T with steps of 5 mT. To maintain identical initial magnetic states, we saturate the sample at negative field H_i for each successive iteration with the new H_m . We note that inverting the sign of the saturation field ($\mu_0 H_i = +1.8$ T) yields identical remanent magnetization.

As follows from Fig. 1(b), for any tilt angle with increasing H_m the remanent magnetization reaches a plateau. For $\theta < 85^\circ$, the remanent magnetization shows a clear peak shortly before the plateau. With increasing θ , the peak and the plateau shift towards higher magnetic fields because the IP saturation field is larger than the OOP saturation field [Fig. 1(a)]. We obtain the largest value of M_r at $\theta = 75^\circ$. For higher angles, the peak disappears along with an overall reduction of M_r for the whole range of H_m (compare, e.g., the curves for $\theta = 75^\circ$ and 85°).

To verify the domain states across the peak, we performed MFM measurements for the [Co (0.44 nm)/Pt (0.7 nm)]₁₅₀ sample, processed with the DCR protocol, and results are presented in Fig. 2. Figure 2(h) plots the remanent magnetization together with the domain density calculated from the corresponding MFM images shown in Figs. 2(a)–2(g). The domain states are stabilized at fixed $\theta = 60^\circ$ for different H_m in the vicinity of the peak. It is quite evident that the remanent magnetization can be used as a direct measure for tracking the domain density. The peak of M_r in Fig. 2(h) corresponds to the densest bubble state, seen in the MFM image at remanence after applying the external field $\mu_0 H_m = 0.9$ T [Fig. 2(d)]. Notably, all MFM images show an alignment of the elongated domains parallel to the IP component of the magnetic field, which indicates the coupling of magnetization within the

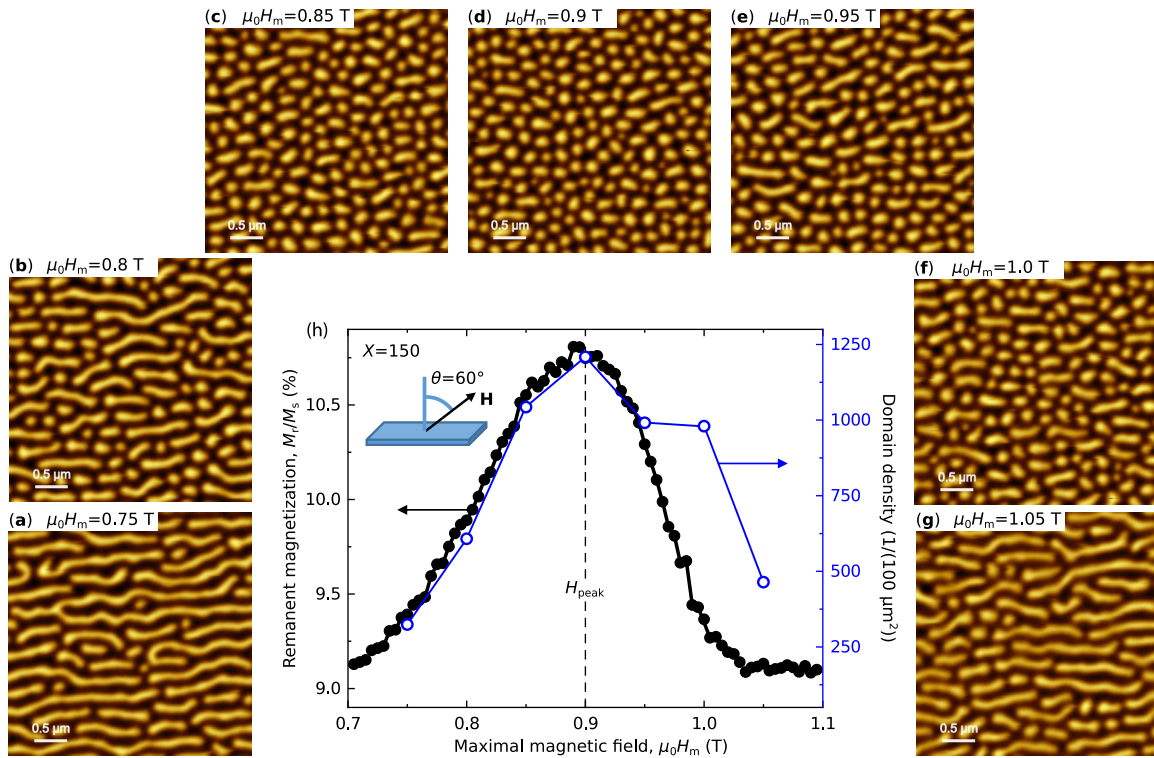


FIG. 2. (a)–(g) MFM images recorded at zero magnetic field after the application of different magnetic fields H_m (DCR protocol) at $\theta = 60^\circ$ with respect to the $[\text{Co} (0.44 \text{ nm})/\text{Pt} (0.7 \text{ nm})]_{150}$ film normal. The dense bubble state for $\mu_0 H_m = 0.9$ T in (d) is evident. (h) Normalized remanent magnetization (black circles) and magnetic domain density (blue circles) as a function of previously applied magnetic field (H_m) in the DCR protocol for the field angle $\theta = 60^\circ$. Note that the black curve is the enlarged view of the red curve in Fig. 1(b). The domain density (blue circles) is calculated from the corresponding MFM images (a)–(g). It is visible that the remanent magnetization mimics the domain density.

Bloch-type domain walls to the IP component of the external field [39].

To identify the optimal tilt angle, in Fig. 3(i) we plot maximal M_r/M_s (black circles) and the domain density (blue open circles) as a function of magnetic field angles varying between $\theta = 0^\circ$ and 90° . Note that each point in the plot corresponds to M_r/M_s at the H_{peak} for each individual θ . The bottom-right inset in Fig. 3(i) shows the dependence of H_{peak} on the angle θ . Since at $\theta < 10^\circ$ and $\theta > 85^\circ$ the dependence $M_r(H_m)$ has no peak, in these cases for H_{peak} the magnetic field at saturation is chosen, displayed by hollow circles. Following the angle θ , one sees that the domains in the MFM images [Figs. 3(a)–3(h)] evolve from long stripes at $\theta = 45^\circ$ to a mixture of short stripes and bubbles at $\theta = 55^\circ$ and 60° . With a further increase of θ , we reach an almost pure bubble state at $\theta = 65^\circ$, and with the subsequent increase of the tilt angle up to $\theta = 75^\circ$, magnetic bubbles decrease in size leading to an even larger bubble density. Thus, by adjusting the field angle, one can control the bubble size and, accordingly, the bubble density. The fact that the remanent magnetization mimics the domain density is also evident from the matching of the angular dependencies of the remanent magnetization and the domain density in Fig. 3(i). The higher the asymmetry between up and down remanent domain areas, the higher is the resulting remanent magnetization. The highest symmetry and lowest magnetization are reached in a labyrinth stripe domain state. The highest asymmetry is obtained in a dense bubble

state, where lots of domains of one polarity are surrounded by a single interconnected domain of the other polarity. This very frustrated state has the highest remanent magnetization and is stabilized by the magnetostatic repulsion of the bubbles. Due to this relationship between remanent moment and micromagnetic domain state, the remanent magnetization is a very reliable indicator for the presence of magnetic bubble states.

To verify the applicability of our approach for bubble states in different ML systems, we use the same DCR protocol for thinner $[\text{Co} (0.44 \text{ nm})/\text{Pt} (0.7 \text{ nm})]_X$ samples with $X = 100$ and 48 . The corresponding MFM images, bubble densities ρ_b , and size distributions for bubbles, stabilized at $\theta = 60^\circ$ and 75° , are displayed in Fig. 4 for all samples. The equivalent bubble diameter is calculated from the domain area, assuming a circular shape. All distributions show characteristic peaks, which we fit using a single Gaussian profile. The fit parameters are summarized in Table I. It is apparent that the bubble domain size decreases with decreasing film thickness as expected for MLs with PMA in this thickness regime [27,28,47]. The highest bubble density is obtained for the $X = 48$ sample at an angle of $\theta = 75^\circ$ [Figs. 4(i) and 4(l)] with $\rho_b = 3736$ domains per $100 \mu\text{m}^2$. All samples reveal that the mean bubble diameter, D_b , for states stabilized at larger field angles ($\theta = 75^\circ$) is smaller than for states stabilized at smaller angles ($\theta = 60^\circ$). The latter states, however, show a narrower size distribution, as indicated by the full width at half-maximum

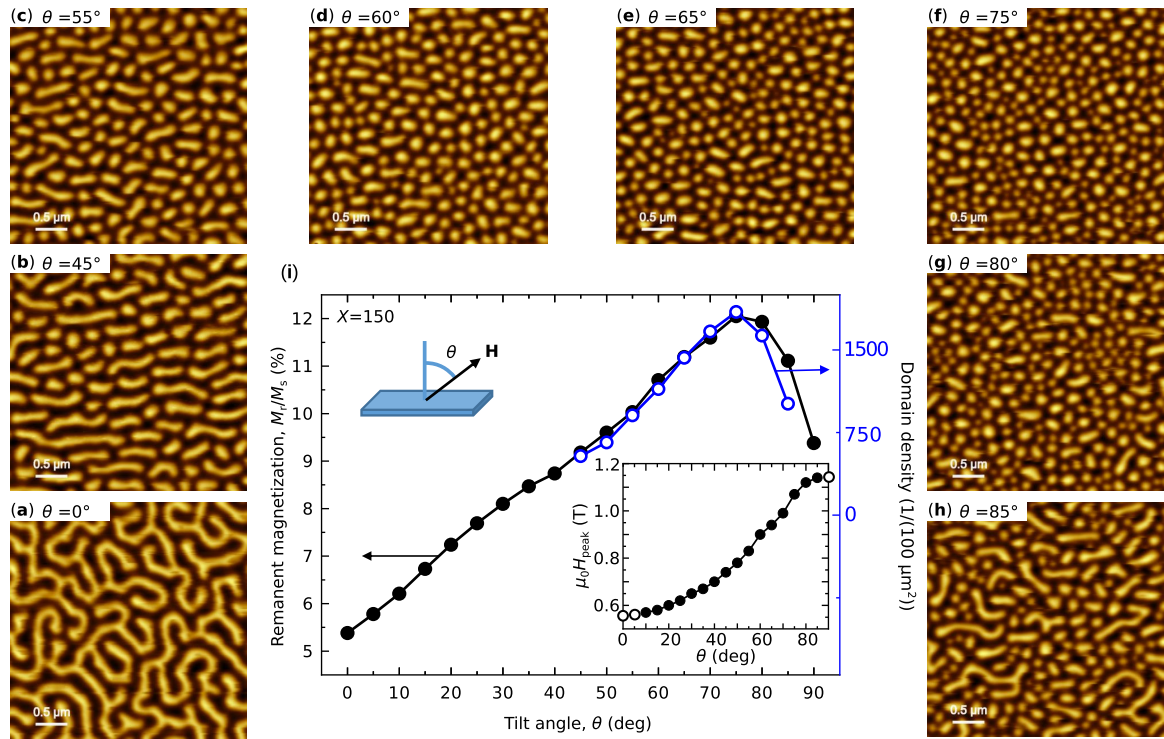


FIG. 3. (a)–(h) Zero-field MFM images, recorded after the DCR protocol for magnetic fields, $H_m = H_{\text{peak}}$, which correspond to the maximum remanent magnetization at particular magnetic field angles θ in the $[\text{Co} (0.44 \text{ nm})/\text{Pt} (0.7 \text{ nm})]_{150}$ ML. (i) Maximal remanent magnetization (black circles) and corresponding magnetic domain density (blue open circles) for different θ in the DCR measurements. The domain density is calculated from the corresponding MFM images shown in (b)–(h). The inset shows the magnetic fields $H_m = H_{\text{peak}}$ as a function of θ .

(w) of the Gaussian profile (see Table I). We obtain the smallest bubble diameter ($D_b = 125 \text{ nm}$) in the $X = 48$ sample; however, the bubble size distribution remains broad ($w = 65 \text{ nm}$). A small portion of bubbles with a diameter of about 50 nm can be stabilized using the DCR protocol at $\theta = 75^\circ$. To illuminate the physical origin of the broad size distribution of bubble domains in our samples, we perform micromagnetic simulations using the mumax code [48].

IV. MICROMAGNETIC SIMULATIONS

For micromagnetic simulations, we use a simulated domain of a square shape in the xy -plane with size $L_x = L_y = 464 \text{ nm}$ and thickness $L_z = 54.72 \text{ nm}$, which is approximately the thickness of the ML with $X = 48$. The sample size is chosen to fit two equilibrium stripe-domain periods of 164 nm along the diagonal of a square domain. The mesh density in our simulations is $256 \times 256 \times 48$ cuboids. We use periodic boundary conditions in the xy -plane and parametrize the direction of the applied magnetic field by polar angle θ and azimuthal angle φ . Figure 5(a) illustrates the geometry of the simulated domain structure with the maze-like stripe domain state, obtained after energy minimization at random distribution of magnetization in the initial state and $\theta = 0^\circ$. The obtained stripe domain pattern mimics the maze-like domain texture observed in the experiment, as shown in the top left inset in Fig. 1(a). We use an approximation of continuum anisotropic media, which represents an extension of the earlier used model in Ref. [39]. Since the coupling between Co layers across Pt layers is

weaker than the direct exchange within the Co layer, we assume that the exchange interaction is anisotropic. In this case, the Heisenberg exchange interaction in the micromagnetic energy density functional can be written as

$$w_{\text{ex}} = A \sum_i \left[\left(\frac{\partial m_i}{\partial x} \right)^2 + \left(\frac{\partial m_i}{\partial y} \right)^2 + k_{\text{iec}} \left(\frac{\partial m_i}{\partial z} \right)^2 \right], \quad (1)$$

where $\mathbf{m} = \mathbf{M}/M_s$ is the magnetization unit vector field, and the summation runs over the spatial coordinates $i = x, y, z$. The constant A stands for the exchange coupling in the plane of the film, while the parameter k_{iec} defines the weakening of the exchange coupling in the vertical direction due to the Co/Pt multilayering. In the simulations, which also include demagnetizing field effects, we use the experimentally estimated values for saturation magnetization, $M_s = 0.775 \text{ MA/m}$, uniaxial anisotropy constant, $K_u = 0.6 \text{ MJ/m}^3$, and the unitless constant $k_{\text{iec}} = 0.2$, which was estimated earlier in Ref. [39] for similar multilayer systems. In the following, we assume that the film has a granular structure, as illustrated in Fig. 5(b). The grains have an average lateral size of 25 nm and penetrate through the whole film thickness. This assumption is justified by many experimental studies that confirm column-like shapes of the grains in Co/Pt multilayers [33–37]. It is assumed that the anisotropy axis in different grains deviates from the perpendicular direction [Figs. 5(c) and 5(d)]. The deviation of the polar angle of the vector \mathbf{K}_u is described by a normal distribution, while the azimuthal angle is uniformly distributed across the interval $[0, 2\pi)$. Such an assumption

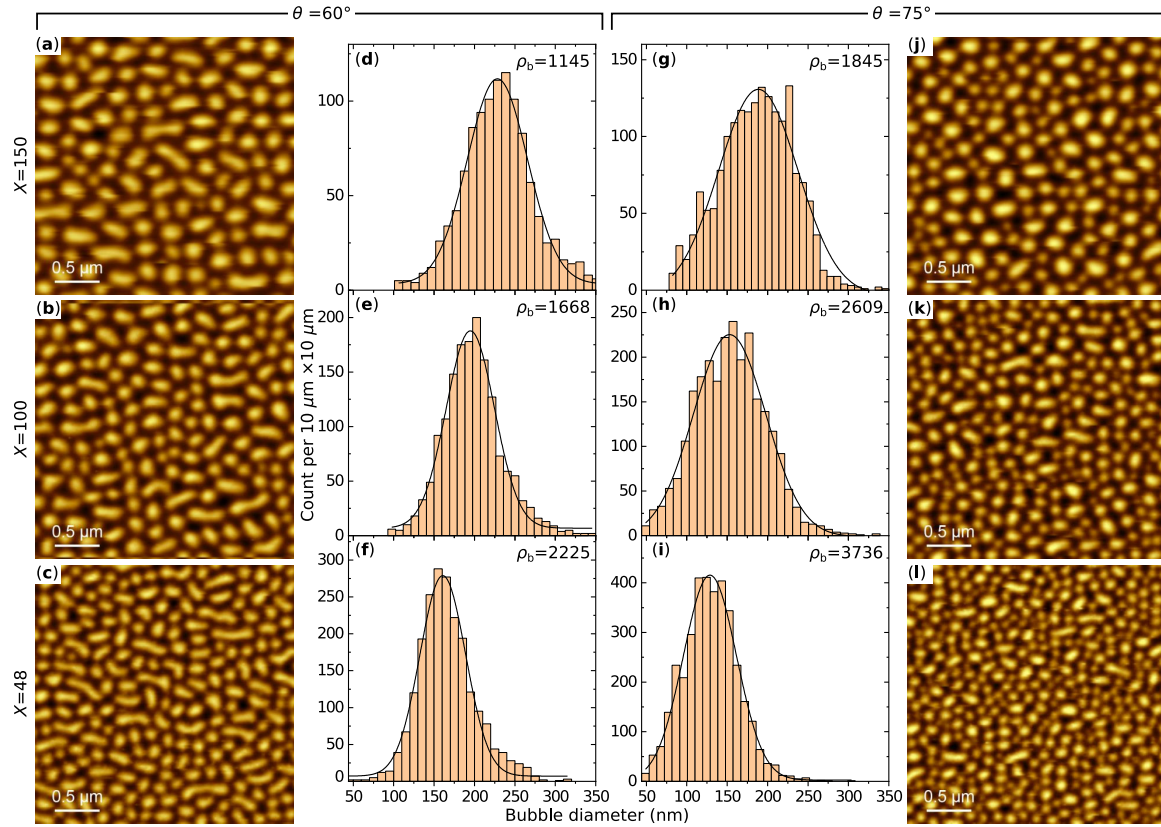


FIG. 4. (a)–(c) MFM images and (d)–(f) size distribution histograms (which include the density of domains ρ_b per $100 \mu\text{m}^2$) for magnetic bubbles stabilized at a magnetic field angle of $\theta = 60^\circ$ in $[\text{Co} (0.44 \text{ nm})/\text{Pt} (0.7 \text{ nm})]_X$ MLs with $X = 150$ (a), (d); 100 (b), (e); and 48 (c), (f). The black solid curve in (d)–(f) represents the fit to the size distribution using a single Gaussian profile. The Gaussian profile is used for obtaining statistical characteristics, i.e., average bubble diameter D_b and distribution width w as summarized in Table I. (g)–(i) The size distribution histograms for bubbles stabilized at $\theta = 75^\circ$, and (j)–(l) corresponding MFM images for samples with $X = 150$ (g), (j); 100 (h), (k); and 48 (i), (l). The solid lines in (g)–(i) represent a single Gaussian fit, which shows smaller D_b but broader size distribution as compared to bubbles stabilized at $\theta = 60^\circ$.

of the anisotropy axes is justified by the columnar grain growth in polycrystalline MLs, which triggers a wavy surface morphology, known as a correlated roughness in multilayered films, grown by magnetron sputter deposition [32–37]. The justification of the granular model can also be found in the works by Schrefl and co-workers [49,50].

The absolute value of the anisotropy K_u is fixed in all grains. We found that variation of K_u over the grains causes the theoretical magnetization curves to deviate from the experimentally measured ones. We also tested the role of intergranular coupling, and we concluded that in the case of the

multilayers studied here, the small variation of intergranular coupling does not affect the system behavior. On the other hand, a significantly reduced intergranular coupling enhances the hysteretic effects, which are almost completely absent in our experimental magnetization curves. In conclusion, only the anisotropy axis variation across the grains was found to be a necessary condition for successfully simulating the experimentally observed magnetization reversal. In contrast, an assumed distribution of the absolute value of anisotropy or intergrain coupling by themselves cannot explain the domain behavior observed in our experiments. For details of the above analysis and implementation of the model in mumax, we refer the reader to the script and simulated curves provided in the Supplemental Material [31].

The representative results of the micromagnetic calculations are displayed in Fig. 6. We consider the case of a magnetic field tilt angle $\theta = 60^\circ$ and $\varphi = 45^\circ$. First, we simulated a major magnetization loop with maximal field ± 1.5 T. We start with the negative saturation at -1.5 T, then we gradually increase the field in steps of 0.01 T and minimize the energy at each step; see the blue curve in Fig. 6(a). After reaching nearly the saturated state at $+1.5$ T, we gradually decrease the field with the same steps; see the red curve. We collect snapshots of the magnetization vector field at each

TABLE I. The total ML film thickness, the mean value of diameter D_b , and the size distribution width w for magnetic bubbles stabilized at $\theta = 60^\circ$ and 75° field angles in $[\text{Co} (0.44 \text{ nm})/\text{Pt} (0.7 \text{ nm})]_X$ MLs with $X = 48, 100$, and 150 .

Sample	ML thickness	$\theta = 60^\circ$		$\theta = 75^\circ$	
		D_b (nm)	w (nm)	D_b (nm)	w (nm)
$X = 48$	55 nm	160 ± 15	55 ± 10	125 ± 10	65 ± 10
$X = 100$	114 nm	185 ± 15	55 ± 10	145 ± 15	85 ± 10
$X = 150$	171 nm	225 ± 15	75 ± 10	180 ± 15	95 ± 15

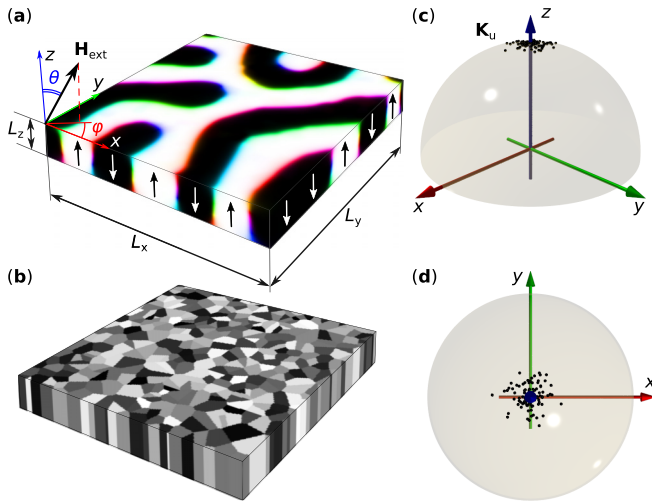


FIG. 5. (a) Simulated domain of square shape with $L_x = L_y = 464$ nm and thickness $L_z = 54.72$ nm. The external magnetic field orientation is parametrized by angles θ and φ . Part (b) illustrates the underlying grained structure of the film with an average grain size of 25 nm in the xy -plane. The grains penetrate through the whole thickness. (c), (d) Representative distribution of uniaxial anisotropy axes in different grains approximated by a normal distribution. For details, see the main text and mumax script in the Supplemental Material [31].

field step. Some representative images of the magnetization in the middle plane of the simulated box are shown in the insets in Fig. 6(a). Bright and dark contrast indicate positive and negative z -component of magnetization, respectively. We use the standard red-green-blue color code for the in-plane component of magnetization implemented in mumax. For illustrative purposes, all snapshots of the system depicted in Figs. 6(a) and 6(c)–6(e) correspond to the domain of a larger size, $2L_x \times 2L_y$, made by taking into account periodic boundary conditions in the xy -plane. The actual size of the simulated domain is indicated for reference by the red dashed square in the inset for $H = -1.2$ T in Fig. 6(a).

As follows from the snapshots in Fig. 6(a), after the saturation at a high magnetic field, the magnetic textures at zero field always represent a mixture of elongated and short domains. Note, because of the random distribution of the anisotropy axis, and finite precision of numerical operations in the computer simulations, the magnetic states at remanence are similar but not identical; compare the two insets for zero field. One can also see that the elongated stripe domains are typically aligned with the in-plane projection of the external magnetic field. At about 0.4 T, the system tends to form a regular stripe domain pattern. With increasing the field, the regular stripe domains split into isolated domains; see the inset for 0.8 T. The density of domains per unit area varies with the field. Approaching the field of 1.1 T, most of the domains collapse and only a small fraction of the domains survives above that critical field. That is illustrated, for instance, by the inset for -1.2 T in Fig. 6(a). Approaching fields of ± 1.5 T, even these domains disappear.

To simulate the experimental measurements of the remanent magnetization, we perform the following steps. We start

the simulations at different positive magnetic fields, H_m , and initial states corresponding to the snapshot of the system at the increasing branch of the magnetization loop [Fig. 6(a)]. The snapshots of these states are depicted in the top row of the images in Figs. 6(c) and 6(d). Next, we perform the energy minimization with gradually decreasing field down to zero in steps of 0.01 T. The examples of the resulting minor magnetization curves are provided in the Supplemental Material [31]. The remanent magnetization of the system in the projection on the field direction for different maximal fields H_m is shown in Fig. 6(b), and the corresponding snapshots of the system at maximal field and at remanence are provided in Figs. 6(c) and 6(d). In agreement with the experimental observation, the theoretical dependence of $M_r(H_m)$ has a distinct maximum at ~ 0.8 T. As follows from the snapshots in Figs. 6(c) and 6(d), the domain density per simulated domain structure is maximal at this value of H_m as well as after reduction of the field down to zero. For $H_m < 0.8$ T, the remanent magnetization and the domain density decay continuously. On the other hand, with H_m exceeding the critical value ~ 1.1 T, the remanent magnetization converges to a constant value of $\sim 8.8\%$ of saturation magnetization M_s , which also agrees well with the experimental observations.

In addition to the consistency with in-field observations, the grained structure also explains the broad distribution of domain sizes depicted in Fig. 4, at least on a qualitative level. To illustrate the role of the grained structure on the domain size distribution, we performed the energy minimization of the magnetic texture shown in the bottom row of the images in Fig. 6(d), with setting the uniaxial anisotropy parallel to the z -axis in all grains, which effectively corresponds to an absence of the grain structure. The resulting domain profile is shown in Fig. 6(e). It becomes apparent that in the absence of the grains, the system tends to have more regular domains of identical shape and size. The latter is most prominent for $H_m = 0.8$ T, where, in the absence of grains, the system converges to a regular closest packed quasihexagonal lattice of magnetic bubble domains. In this case, the bubbles are slightly elongated only because the square-shaped simulated domain is not perfectly commensurate with the period of the hexagonal bubble lattice.

It is worth noting that at a high magnetic field, all domains are type II bubbles [12]; see the top row of the images in Fig. 6(d). With decreasing the external field to zero, most of these domains converge to a transient state with a pair of Bloch points and then transit into topologically nontrivial type I bubbles at negative magnetic fields. Such a topological transition represents an interesting phenomenon that is beyond the scope of the present study and will be discussed elsewhere.

The agreement between theoretical and experimental results allows us to conclude that the formation of a dense bubble domain lattice under tilted external magnetic fields can be effectively explained by the underlying granular structure of magnetic multilayers synthesized by magnetron sputter deposition. Without the implementation of the grained structure with anisotropy axis variation, neither the magnetization curve nor magnetic configurations show agreement with the experimental observations. For instance, the spontaneous nucleation of domains, in this case, takes place in a reverse field only. It is worth noting that the splitting of the stripe domains into

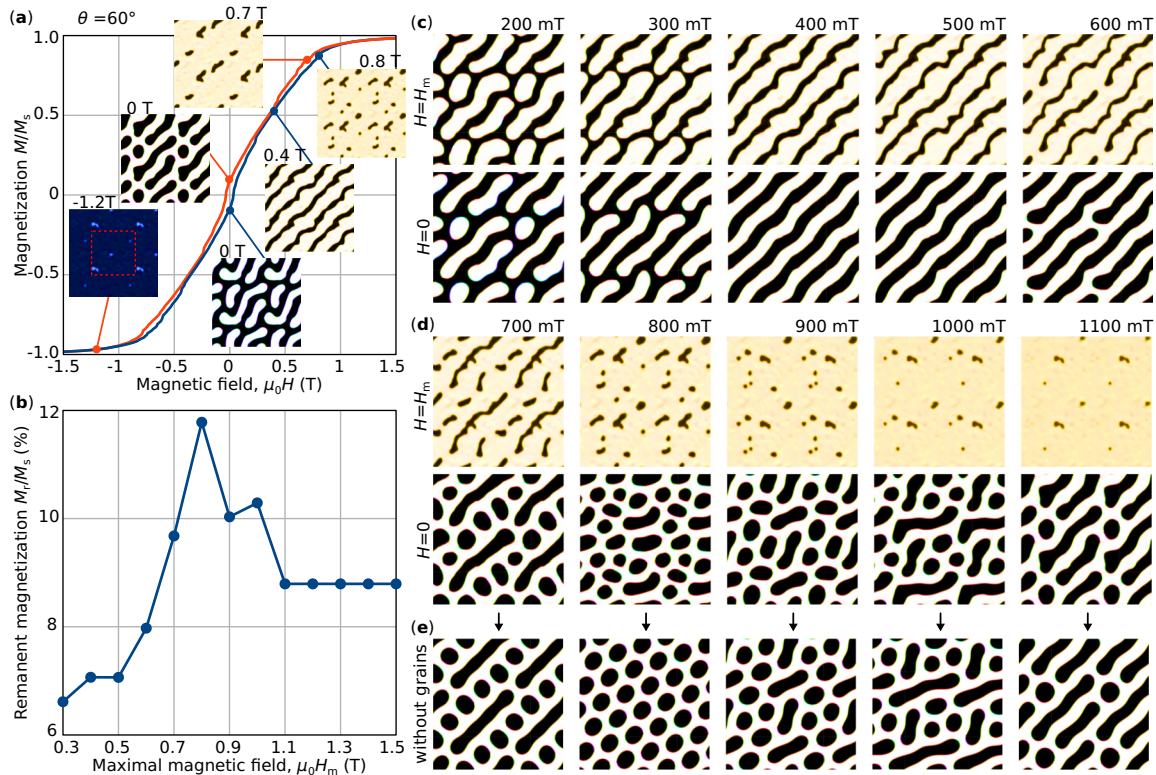


FIG. 6. (a) Magnetization loop obtained in micromagnetic simulations at $\theta = 60^\circ$ and $\varphi = 45^\circ$. The insets show the snapshots of the magnetization in the center plane of the film. (b) Theoretically estimated dependence of the remanent magnetization as a function of the previously applied maximal magnetic field. Each pair of images in (c) and (d) has the following meaning: the top image illustrates the magnetization in the middle plane at the maximal magnetic field, while the bottom image shows the state after gradual field reduction to zero. The remanent magnetization of these states is shown in (b). The images in (e) illustrate the states obtained after full energy minimization with the initial configuration as in the bottom row in (d) and with setting the anisotropy axis in each grain to be parallel to the z -axis, which is effectively equivalent to the grains being absent, i.e., the case of an isotropic medium in the xy -plane.

individual bubbles in the model without grains also takes place [20,27,40,41]. However, the transition fields turn out to be very sensitive to nonphysical parameters of the model, such as mesh density or field step. Transitions of that kind are typically ignored as numerical artifacts. Moreover, the absolute values of the transition fields between stripes and type II bubbles in the model without grains are much higher than the experimental values. On the contrary, even a quite simplified model of the grain structure provides quantitative agreement with experimental observations.

V. CONCLUSIONS

In conclusion, we demonstrate an approach for the stabilization of magnetic bubble states in metallic ML films with strong PMA ($Q > 1$). The approach is based on monitoring the remanent magnetization while performing systematic magnetic field protocols at different tilt angles with respect to the film's surface. We demonstrate that the remanent magnetization mimics the domain density, showing a distinct peak for the densest bubble state achievable, which corresponds here for the $X = 48$ sample to a bubble density of 3736 domains/ $100 \mu\text{m}^2$. Furthermore, our approach allows the identification of different types of bubble states at ambient

conditions within one and the same sample. These states are characterized by different mean bubble sizes and size distribution. These characteristics can be tuned by choosing a suitable magnetic field angle and amplitude. The micromagnetic modeling provides a quantitative agreement with experimental observations and suggests that the granular structure with a grainwise variation in anisotropy direction of the MLs is responsible for the broad distribution of domain sizes observed experimentally. This implies that by aiming at a more homogeneous microstructure of the PMA MLs, for example by using amorphous systems, the broad bubble size distribution may be avoided. In turn, the bubble states of different diameters and with a broad size distribution may, in combination with different domain-wall topological states, turn out to be useful as multidimensional magnetic memory for artificial neural networks [51]. Our work provides the foundation for further exploration of topological switching of DWs in dipolar bubbles, which are stabilized in metallic MLs at room temperature and zero magnetic field.

ACKNOWLEDGMENT

The authors are grateful to Thomas Naumann and Jakob Heinze for experimental and technical support.

- [1] M. Sharad, C. Augustine, G. Panagopoulos, and K. Roy, Spin-based neuron model with domain-wall magnets as synapse, *IEEE Trans. Nanotechnol.* **11**, 843 (2012).
- [2] Y. Huang, W. Kang, X. Zhang, Y. Zhou, and W. Zhao, Magnetic skyrmion-based synaptic devices, *Nanotechnology* **28**, 08LT02 (2017).
- [3] Z. Yu, M. Shen, Z. Zeng, S. Liang, Y. Liu, M. Chen, Z. Zhang, Z. Lu, L. You, X. Yang *et al.*, Voltage-controlled skyrmion-based nanodevices for neuromorphic computing using a synthetic antiferromagnet, *Nanoscale Adv.* **2**, 1309 (2020).
- [4] N. Nagaosa and Z. Tokura, Topological properties and dynamics of magnetic skyrmions, *Nat. Nanotechnol.* **8**, 899 (2013).
- [5] A. Fert, V. Cros, and J. Sampaio, Skyrmions on the track, *Nat. Nanotechnol.* **8**, 152 (2013).
- [6] R. Tomasello, E. Martinez, R. Zivieri, L. Torres, M. Carpentieri, and G. Finocchio, A strategy for the design of skyrmion race-track memories, *Sci. Rep.* **4**, 6784 (2015).
- [7] S. Woo, K. Litzius, B. Krüger, M.-Y. Im, L. Caretta, K. Richter, M. Mann, A. Krone, R. M. Reeve, M. Weigand *et al.*, Observation of room-temperature magnetic skyrmions and their current-driven dynamics in ultrathin metallic ferromagnets, *Nat. Mater.* **15**, 501 (2016).
- [8] K. Litzius, I. Lemesh, B. Krüger, P. Bassirian, L. Caretta, K. Richter, F. Büttner, K. Sato, O. A. Tretiakov, J. Förster *et al.*, Skyrmion Hall effect revealed by direct time-resolved X-ray microscopy, *Nat. Phys.* **13**, 170 (2017).
- [9] W. Jiang, X. Zhang, G. Yu, W. Zhang, X. Wang, M. B. Jungfleisch, J. E. Pearson, X. Cheng, O. Heinonen, K. L. Wang *et al.*, Direct observation of the skyrmion Hall effect, *Nat. Phys.* **13**, 162 (2017).
- [10] G. Yu, P. Upadhyaya, Q. Shao, H. Wu, G. Yin, X. Li, C. He, W. Jiang, X. Han, P. K. Amiri, and K. L. Wang, Room-temperature skyrmion shift device for memory application, *Nano Lett.* **17**, 261 (2017).
- [11] W. Legrand, D. Maccariello, N. Reyren, K. Garcia, C. Moutafis, C. Moreau-Luchaire, S. Collin, K. Bouzehouane, V. Cros, and A. Fert, Room-temperature current-induced generation and motion of sub-100 nm skyrmions, *Nano Lett.* **17**, 2703 (2017).
- [12] A. P. Malozemoff and J. C. Slonczewski, *Magnetic Domain Walls in Bubble Materials* (Academic Press, New York, 1979).
- [13] N. S. Kiselev, A. N. Bogdanov, R. Schafer, and U. K. Rößler, Chiral skyrmions in thin magnetic films: New objects for magnetic storage technologies? *J. Phys. D* **44**, 392001 (2011).
- [14] P. Milde, D. Köhler, J. Seidel, L. M. Eng, A. Bauer, A. Chacon, J. Kindervater, S. Mühlbauer, C. Pfleiderer, S. Buhrandt *et al.*, Unwinding of a skyrmion lattice by magnetic monopoles, *Science* **340**, 1076 (2013).
- [15] C. Moutafis, S. Komineas, and J. A. C. Bland, Dynamics and switching processes for magnetic bubbles in nanoelements, *Phys. Rev. B* **79**, 224429 (2009).
- [16] W. Koshibae and N. Nagaosa, Berry curvature and dynamics of a magnetic bubble, *New J. Phys.* **18**, 045007 (2016).
- [17] Y. Yamane and J. Sinova, Skyrmion-number dependence of spin-transfer torque on magnetic bubbles, *J. Appl. Phys.* **120**, 233901 (2016).
- [18] W. Koshibae and N. Nagaosa, Theory of skyrmions in bilayer systems, *Sci. Rep.* **7**, 42645 (2017).
- [19] N. Ogawa, W. Koshibae, A. J. Beekman, N. Nagaosa, M. Kubota, M. Kawasaki, and Y. Tokura, Photodrive of magnetic bubbles via magnetoelastic waves, *Proc. Natl. Acad. Sci. USA* **112**, 8977 (2015).
- [20] S. A. Montoya, S. Couture, J. J. Chess, J. C. T. Lee, N. Kent, D. Henze, S. K. Sinha, M.-Y. Im, S. D. Kevan, P. Fischer *et al.*, Tailoring magnetic energies to form dipole skyrmions and skyrmion lattice, *Phys. Rev. B* **95**, 024415 (2017).
- [21] S. A. Montoya, S. Couture, J. J. Chess, J. C. T. Lee, N. Kent, M.-Y. Im, S. D. Kevan, P. Fischer, B. J. McMorrin, S. Roy *et al.*, Resonant properties of dipole skyrmions in amorphous Fe/Gd multilayers, *Phys. Rev. B* **95**, 224405 (2017).
- [22] K. Pátek, R. Gemperle, L. Murtinová, and J. Kaczér, Magnetization reversal and Bloch lines in bubble domain walls, *J. Magn. Magn. Mater.* **123**, 223 (1993).
- [23] A. Hubert and R. Schäfer, *Magnetic Domains* (Springer, Berlin, 2009).
- [24] B. Lyu, W. Wang, and H. Du, Magnetic bubble dynamics driven by magnetic field gradients, *J. Magn. Magn. Mater.* **541**, 168475 (2022).
- [25] Z. Hou, Q. Zhang, X. Zhang, G. Xu, J. Xia, B. Ding, H. Li, S. Zhang, N. M. Batra, P. M. F. J. Costa *et al.*, Current-induced helicity reversal of a single skyrmionic bubble chain in a nanostructured frustrated magnet, *Adv. Mater.* **32**, 1904815 (2020).
- [26] Y. Wu, L. Kong, Y. Wang, J. Li, Y. Xiong, and J. Tang, A strategy for the design of magnetic memories in bubble-hosting magnets, *Appl. Phys. Lett.* **118**, 122406 (2021).
- [27] K. Chesnel, A. S. Westover, C. Richards, B. Newbold, M. Healey, L. Hindman, B. Dodson, K. Cardon, D. Montealegre, J. Metzner *et al.*, Morphological stripe-bubble transition in remanent magnetic domain patterns of Co/Pt multilayer films and its dependence on Co thickness, *Phys. Rev. B* **98**, 224404 (2018).
- [28] L. Fallarino, A. Oelschlägel, J. A. Arregi, A. Bashkatov, F. Samad, B. Böhm, K. Chesnel, and O. Hellwig, Control of domain structure and magnetization reversal in thick Co/Pt multilayers, *Phys. Rev. B* **99**, 024431 (2019).
- [29] R. D. Desautels, L. DeBeer-Schmitt, S. A. Montoya, J. A. Borchers, S.-G. Je, N. Tang, M.-Y. Im, M. R. Fitzsimmons, E. E. Fullerton, and D. A. Gilbert, Realization of ordered magnetic skyrmions in thin films at ambient conditions, *Phys. Rev. Mater.* **3**, 104406 (2019).
- [30] S.-G. Je, H.-S. Han, S. K. Kim, S. A. Montoya, W. Chao, I.-S. Hong, E. E. Fullerton, K.-S. Lee, K.-J. Lee, M.-Y. Im, and J.-I. Hong, Direct demonstration of topological stability of magnetic skyrmions via topology manipulation, *ACS Nano* **14**, 3251 (2020).
- [31] See Supplemental Material at <http://link.aps.org/supplemental/10.1103/PhysRevB.106.054404> for magnetic hysteresis and x-ray reflectivity data for all samples as well as the mumax script and additional figures, which illustrate the comparison of theoretical and experimental magnetization curves and minor magnetization curves obtained in micromagnetic simulations.
- [32] Zs. Czigany and G. Radnoczi, Columnar growth structure and evolution of wavy interface morphology in amorphous and polycrystalline multilayered thin films, *Thin Solid Films* **347**, 133 (1999).
- [33] P. He, W. A. McGaham, S. Nafis, J. A. Woollam, Z. S. Shan, and S. H. Liou, Sputtering pressure effect on microstructure of surface and interface, and on coercivity of Co/Pt multilayers, *J. Appl. Phys.* **70**, 6044 (1991).

- [34] D. Weller, L. Folks, M. Best, E. E. Fullerton, and B. D. Terris, Growth, structural, and magnetic properties of high coercivity Co/Pt multilayers, *J. Appl. Phys.* **89**, 7525 (2001).
- [35] M. S. Pierce, J. E. Davies, J. J. Turner, K. Chesnel, E. E. Fullerton, J. Nam, R. Hailstone, S. D. Kevan, J. B. Kortright, K. Liu *et al.*, Influence of structural disorder on magnetic domain formation in perpendicular anisotropy thin films, *Phys. Rev. B* **87**, 184428 (2013).
- [36] Y. S. Chen, A.-C. Sun, H. Y. Lee, H.-C. Lu, S.-F. Wang, and P. Sharma, Enhanced coercivity of HCP Co–Pt alloy thin films on a glass substrate at room temperature for patterned media, *J. Magn. Magn. Mater.* **391**, 12 (2015).
- [37] B. Böhm, L. Fallarino, D. Pohl, B. Rellinghaus, K. Nielsch, N. S. Kiselev, and O. Hellwig, Antiferromagnetic domain wall control via surface spin flop in fully tunable synthetic antiferromagnets with perpendicular magnetic anisotropy, *Phys. Rev. B* **100**, 140411(R) (2019).
- [38] J. E. Davies, O. Hellwig, E. E. Fullerton, G. Denbeaux, J. B. Kortright, and K. Liu, Magnetization reversal of Co/Pt multilayers: Microscopic origin of high-field magnetic irreversibility, *Phys. Rev. B* **70**, 224434 (2004).
- [39] R. Salikhov, F. Samad, B. Böhm, S. Schneider, D. Pohl, B. Rellinghaus, A. Ullrich, M. Albrecht, J. Lindner, N. S. Kiselev, and O. Hellwig, Control of Stripe-Domain-Wall Magnetization in Multilayers Featuring Perpendicular Magnetic Anisotropy, *Phys. Rev. Appl.* **16**, 034016 (2021).
- [40] X. Yu, M. Mostovoy, Y. Tokunaga, W. Zhang, K. Kimoto, Y. Matsui, Y. Kaneko, N. Nagaosa, and Y. Tokura, Magnetic stripes and skyrmions with helicity reversals, *Proc. Natl. Acad. Sci. USA* **109**, 8856 (2012).
- [41] Y. Wu, J. Tang, B. Lyu, L. Kong, Y. Wang, J. Li, Y. Soh, Y. Xiong, M. Tian, and H. Du, Stabilization and topological transformation of magnetic bubbles in disks of a kagome magnet, *Appl. Phys. Lett.* **119**, 012402 (2021).
- [42] S. H. Charap and J. M. Nemchik, Behavior of circular domains in GdIG, *IEEE Trans. Magn.* **5**, 566 (1969).
- [43] J. A. Cape and G. W. Lehman, Magnetic domain structures in thin uniaxial plates with perpendicular easy axis, *J. Appl. Phys.* **42**, 5732 (1971).
- [44] N. K. Duong, M. Raju, A. P. Petrovic, R. Tomasello, G. Finocchio, and C. Panagopoulos, Stabilizing zero-field skyrmions in Ir/Fe/Co/Pt thin film multilayers by magnetic history control, *Appl. Phys. Lett.* **114**, 072401 (2019).
- [45] M. Ma, C. C. I. Ang, Y. Li, Z. Pan, W. Gan, W. S. Lew, and F. Ma, Enhancement of zero-field skyrmion density in [Pt/Co/Fe/Ir]₂ multilayers at room temperature by the first-order reversal curve, *J. Appl. Phys.* **127**, 223901 (2020).
- [46] N. K. Duong, R. Tomasello, M. Raju, A. P. Petrovic, S. Chiappini, G. Finocchio, and C. Panagopoulos, Magnetization reversal signatures of hybrid and pure Néel skyrmions in thin film multilayers, *APL Mater.* **8**, 111112 (2020).
- [47] O. Hellwig, A. Berger, J. Kortright, and E. E. Fullerton, Domain structure and magnetization reversal of antiferromagnetically coupled perpendicular anisotropy films, *J. Magn. Magn. Mater.* **319**, 13 (2007).
- [48] A. Vansteenkiste, J. Leliaert, M. Dvornik, M. Helsen, F. Garcia-Sanchez, and B. Van Waeyenberge, The design and verification of MuMax3, *AIP Adv.* **4**, 107133 (2014).
- [49] T. Schrefl, J. Fidler, and H. Kronmüller, Remanence and coercivity in isotropic nanocrystalline permanent magnets, *Phys. Rev. B* **49**, 6100 (1994).
- [50] T. Schrefl, J. Fidler, and J. N. Chapman, Micromagnetic modelling of multilayer media, *J. Phys. D* **29**, 2352 (1996).
- [51] G. Bourianoff, D. Pinna, M. Sitte, and K. Everschor-Sitte, Potential implementation of reservoir computing models based on magnetic skyrmions, *AIP Adv.* **8**, 055602 (2018).